Nano Research 2014, 7(3): 285–300
DOI 10.1007/s12274-014-0403-5
Review Article
ISSN 1998-0124
CN 11-5974/O4

Doping and alloying in atomically precise gold nanoparticles

Rongchao Jin[1] and Katsuyuki Nobusada[2] (✉)

[1] *Department of Chemistry, Carnegie Mellon University, Pittsburgh, Pennsylvania 15213, USA*
[2] *Department of Theoretical and Computational Molecular Science, Institute for Molecular Science, Myodaiji, Okazaki, 444-8585, Japan, and Elements Strategy Initiative for Catalysts and Batteries (ESICB), Kyoto University Katsura, Kyoto 615-8520, Japan*

Received: 24 June 2013
Revised: 13 December 2013
Accepted: 15 December 2013

KEYWORDS
gold nanoparticle,
atomic precision,
total structure,
doping,
alloying

ABSTRACT

The recent success in the synthesis and total structure determination of atomically precise gold nanoparticles has provided exciting opportunities for fundamental studies as well as the development of new applications. These unique nanoparticles are of molecular purity and possess well defined formulas (i.e., specific numbers of metal atoms and ligands), resembling organic compounds. Crystallization of such molecularly pure nanoparticles into macroscopic single crystals allows for the determination of total structures of nanoparticles (i.e., the arrangement of metal core atoms and surface ligands) by X-ray crystallography. In this perspective article, we summarize recent efforts in doping and alloying gold nanoparticles with other metals, including Pd, Pt, Ag and Cu. With atomically precise gold nanoparticles, a specific number of foreign atoms (e.g., Pd, Pt) can be incorporated into the gold core, whereas a range of Ag and Cu substitutions is observed but, interestingly, the total number of metal atoms in the homogold nanoparticle is preserved. The heteroatom substitution of gold nanoparticles allows one to probe the optical, structural, and electronic properties truly at the single-atom level, and thus provides a wealth of information for understanding the intriguing properties of this new class of nanomaterials.

1 Why atomically precise nanoparticles?

Colloidal nanoparticles of metals and semiconductors are being intensely pursued in current nanoscience research. Significant progress has been made in controlling the size and shape of such nanoparticles, and many types of uniform nanoparticles (e.g., with a size distribution of 5%–10%) have become available. Such "high quality" nanoparticles have permitted deep understanding of their size- and shape-dependent properties. However, there are still many fundamental issues that cannot be addressed even with such uniform nanoparticles, for example:

– Why are some types of colloidal nanoparticles particularly stable compared to others?

– What exactly protects the nanoparticles—ligands

Address correspondence to Rongchao Jin, rongchao@andrew.cmu.edu; Katsuyuki Nobusada, nobusada@ims.ac.jp

or surfactants—and how are the particles protected?

In structural studies, transmission electron microscopy (TEM) can reveal the particle morphology (or shape) and permits precise measurements of particle size to a precision of a fraction of a nanometer (e.g., ± 0.2 nm in bright field TEM imaging), but TEM cannot tell what is on the particle surface. On the other hand, spectroscopic tools such as NMR, IR, and Raman scattering offer useful information about the organic components in colloidal nanoparticles, however, such information is often somewhat ambiguous when associated with nanoparticles because colloidal nanoparticles are typically a mixture in which nanoparticles coexist with excess surfactants or ligands, not to mention other possible impurities and byproducts from the synthesis. Even if one can obtain clean nanoparticles (i.e., without free stabilizers, impurities, or side products), such nanoparticles may not be of atomic precision, although they are highly uniform (e.g., with size distribution of 5% that can be obtained in the best cases of conventional syntheses). Therefore, for a given colloid, many simple questions are still difficult to answer; here are some basic questions:

– What species are adsorbed on the surface of colloidal nanoparticles?

– How many atoms does a nanoparticle possess exactly?

– How does the stabilizer (e.g., ligand) protect the particle in terms of bonding mode?

– What determines the stability of nanoparticles?

To address the above simple yet tough questions, a prerequisite is to synthesize atomically precise and molecularly pure nanoparticles. Such unique nanoparticles indeed become "compounds" because they can be assigned a definite formula, rather than a mere size range (e.g., 5 nm ± 0.2 nm). Only with such unprecedented nanoparticles is it possible to reveal their total structure (i.e., the arrangements of metal core atoms and ligands) by single crystal X-ray crystallography and then attempt to understand the properties at the atomic level by correlating with the total structure [1]. This constitutes the major dream of colloid chemists.

Controlling colloidal nanoparticles with atomic precision is by no means an easy task. A very first question is what principle(s) allow one to achieve atomically precise nanoparticles [2]. In recent years, researchers have achieved some breakthroughs in the synthesis of atomically precise gold nanoparticles protected by thiolate ligands, although the size attainable thus far is still limited to the ultrasmall range, e.g., from dozens to several hundreds of metal atoms (with a size of 1–2 nm) [3–10]. The major breakthroughs include the structural determinations of $Au_{25}(SR)_{18}$, $Au_{38}(SR)_{24}$ and $Au_{102}(SR)_{44}$ (which are summarized in Ref. [1]) and the very recently reported face-centered cubic (fcc) structure of $Au_{36}(SR)_{24}$ [9] as well as the establishment of a systematic methodology for the controlled synthesis of such materials [2, 10].

Thiolate-protected gold nanoparticles possess high stability owing to the robust Au–S bonding and thus are particularly attractive in many applications [11–14]. In this Perspective article, we focus on ultrasmall gold nanoparticles (1–2 nm) protected by thiolates. Our interest in gold nanoparticles is also motivated by the questions about the origin of the metallic state—which is essential for the plasmon excitation in gold and other metallic nanoparticles [15]. With decreasing size, the metallic state fades out, so does the plasmon excitation, and quantum effects come into play [4, 16, 17]. Due to the quantum nature of ultrasmall gold nanoparticles, they are also called nanoclusters to be distinguished from their larger counterparts (i.e., plasmonic nanoparticles) [4]. Theoretical treatment of ultrasmall Au nanoparticles requires quantum mechanics [18–23], as opposed to classical physics (e.g., electrodynamics) which is adequate for metallic nanoparticles [24, 25]. Some interesting questions naturally arise about ultrasmall nanoparticles:

– What is the exact nature of the quantum size effect?

– What kind of structure would be adopted in Au nanoclusters other than the fcc structure of bulk gold and plasmonic Au nanoparticles?

Herein we choose a few discrete-size nanoclusters (denoted as $Au_n(SR)_m$, where SR = thiolate) and discuss their structures and properties, with a focus on atomic level manipulations such as doping and alloying by heteroatoms. Substituting one or more gold atoms with heteroatom(s) of other metal elements (such as Pd, Pt, Ag, and Cu) provides exciting opportunities to tune the electronic and optical properties of nanoclusters as well as a deep understanding of the stability of nanoclusters.

2 Doping and alloying in atomically precise nanoparticles

The development of synthetic methods for the preparation and characterization of atomically precise gold nanoparticles with molecular purity has enabled researchers to study the structures and fundamental properties of such nanoparticles at an unprecedented level—the atomic level [1]. First of all, such compound-like nanoparticles allow the growth of single crystals (as opposed to superlattices of nanoparticles) and thus their total structures—not only the arrangement of metal atoms but also of ligands—can be completely solved by X-ray crystallography. Based upon the total structures, many fundamental issues can be addressed and understood [1, 3, 4, 19]. Below we focus on three discrete-size nanoclusters, $Au_{25}(SR)_{18}$, $Au_{38}(SR)_{24}$ and $Au_{144}(SR)_{60}$, and heterometal-substituted bimetal nanoclusters. Other reported sizes such as $Au_{36}(SR)_{24}$ and $Au_{102}(SR)_{44}$ will not be discussed, as no doping work has been done yet. The heteroatom doping in gold nanoclusters allows us to probe the atomic sensitivity of the nanocluster's physical and chemical properties, as well as imparting the nanoclusters with new properties.

2.1 The case of 25-gold atom $Au_{25}(SR)_{18}$ nanoparticles

It is critical to determine the accurate cluster mass by electrospray ionization mass spectrometry (ESI-MS). Based upon the accurate mass, the nanocluster formula can be unambiguously assigned. The $Au_{25}(SR)_{18}$ formula was first determined by Tsukuda and coworkers in 2005 by high resolution ESI-MS [5]. It is worth noting that in earlier work, the formulas of $Au_{28}(SG)_{16}$ (where SG = glutathione) reported by Whetten et al. [16] and $Au_{38}(SCH_2CH_2Ph)_{24}$ by Murray et al. [26] were both incorrect and have been corrected to $Au_{25}(SR)_{18}$ (where SR represent thiolates generally). Subsequently, in 2007–2008, the Murray and Jin groups independently solved the total structure of $Au_{25}(SCH_2CH_2Ph)_{18}$ [27, 28]. The native state of the $Au_{25}(SCH_2CH_2Ph)_{18}$ nanocluster is indeed negatively monocharged (counterion: tetraoctylammonium, TOA^+). Figure 1(a) shows a typical ESI-MS spectrum of molecularly pure $Au_{25}(SCH_2CH_2Ph)_{18}$ nanoparticles; the isotope pattern closely matches the simulated pattern based on the assigned formula (Fig. 1(a), inset), confirming the assignment. The unit cell of the single crystal of $Au_{25}(SCH_2CH_2Ph)_{18}$ nanoparticles contains one particle and its associated TOA^+ counterion (Fig. 1(b)).

Of particular interest are how the metal atoms pack in the nanocluster core and how the thiolate ligands protect the metal core. In the case of $Au_{25}(SR)_{18}$, the Au_{25} metal core comprises a centered icosahedral Au_{13} inner core (or kernel) and an exterior shell of 12 surface Au atoms (Fig. 2) [28]. The Au atoms exhibit three types of environments: the central site (Fig. 2, blue), twelve sites in the icosahedral shell (magenta), and twelve sites in the external surface layer (green).

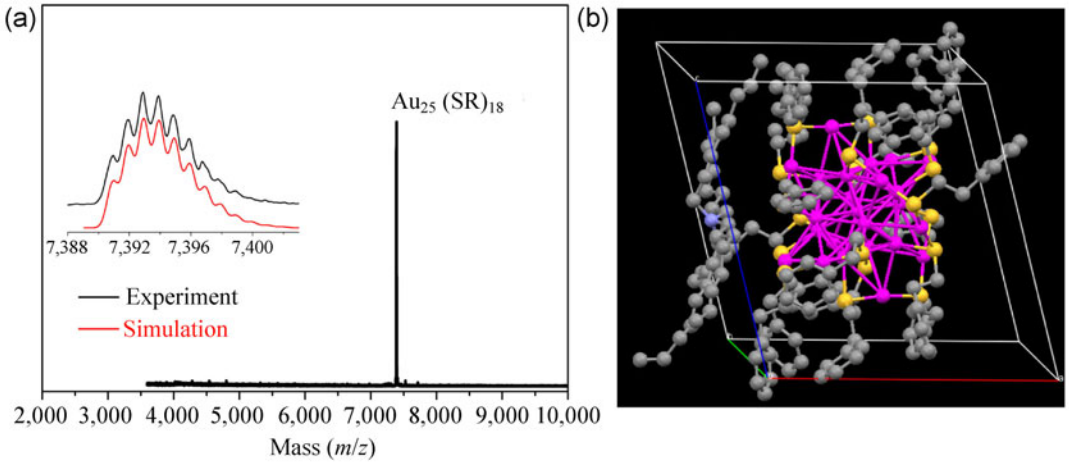

Figure 1 (a) ESI-MS spectrum (negative mode) of $Au_{25}(SR)_{18}$ nanoclusters (in anions, counterion: tetraoctylammonium, TOA^+). (b) Crystal structure of $Au_{25}(SR)_{18}$. Adapted with permission from Ref. [1], Copyright American Chemical Society 2012.

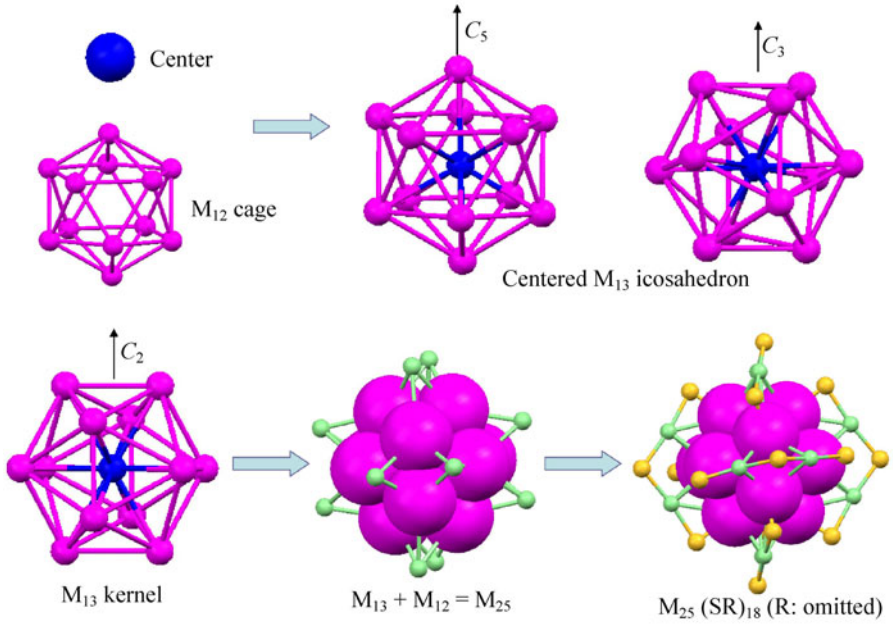

Figure 2 Anatomy of the structure of $Au_{25}(SR)_{18}$ nanoclusters (M = Au, R = CH_2CH_2Ph not shown for clarity). Redrawn from the reported crystal structure file (CIF) of $Au_{25}(SR)_{18}$ nanoclusters.

The Au_{13} icosahedron possesses C_5, C_3 and C_2 rotation axes (Fig. 2). The entire Au_{25} particle is protected by 18 thiolate ligands (Fig. 2, yellow, R omitted). The ligands can be divided into two groups according to their chemical environments (inner vs. outer, Fig. 2) [29–31]. In another view, one may separate the $Au_{25}(SR)_{18}$ structure into an Au_{13} kernel and six –SR–Au–SR–Au–SR– protecting motifs (so-called dimeric "staples", where the prefix (di) refers to the number of gold atoms (two) incorporated into the surface staple motif). It should be emphasized that there is intimate interaction between the Au_{13} kernel and the six dimeric staples, and this interaction is critical for reproducing the optical spectrum of $Au_{25}(SR)_{18}$ in density functional theory (DFT) simulations [28, 32].

With respect to the optical absorption properties of $Au_{25}(SR)_{18}$, three distinct bands in the visible wavelength range were observed at 400, 440, and 680 nm (Fig. 3(a)), which is in striking contrast with the single surface plasmon band of larger, spherical Au nanoparticles. Time-dependent density functional theory (TDDFT) calculations reproduced the experimental spectrum [28], hence the optical transitions can be interpreted. All the optical absorption peaks are associated with single-electron excitations—in distinct contrast with the collective-electron excitation (i.e., plasmons) in larger metallic nanoparticles. Apparently, these one-electron transitions are caused by the significantly quantized electron energy levels (as opposed to quasi-continuous bands in plasmonic nanoparticles). According to TDDFT simulations by Nobusada, the experimental 680 nm peak (Fig. 3(a)) which corresponds to the simulated peak at 660 nm (Fig. 3(b)) is attributed to the HOMO–LUMO transition. Figures 3(c) and 3(d) show the diagrams of HOMO and LUMO of $Au_{25}(SR)_{18}$. Both HOMO and LUMO are mainly constructed from the Au 6p and Au 5d orbitals. However, the HOMO is rather localized around the central Au atom, whereas the LUMO is distributed over the surrounding Au atoms. The second peak at 440 nm is attributed to the transition from the HOMO to the higher Au sp energy band. The monoanionic $Au_{25}(SR)_{18}^{-}$ nanocluster can be readily converted to the charge-neutral form with the Au_{25} framework retained [33], but the optical spectrum exhibits some interesting differences. It is worth noting that the neutral form exhibits paramagnetism [34].

To further probe the electronic and optical properties of $Au_{25}(SR)_{18}$, substitution of gold with heteroatoms has been attempted. Below we discuss four cases, including Pd, Pt, Ag and Cu substitutions. A common

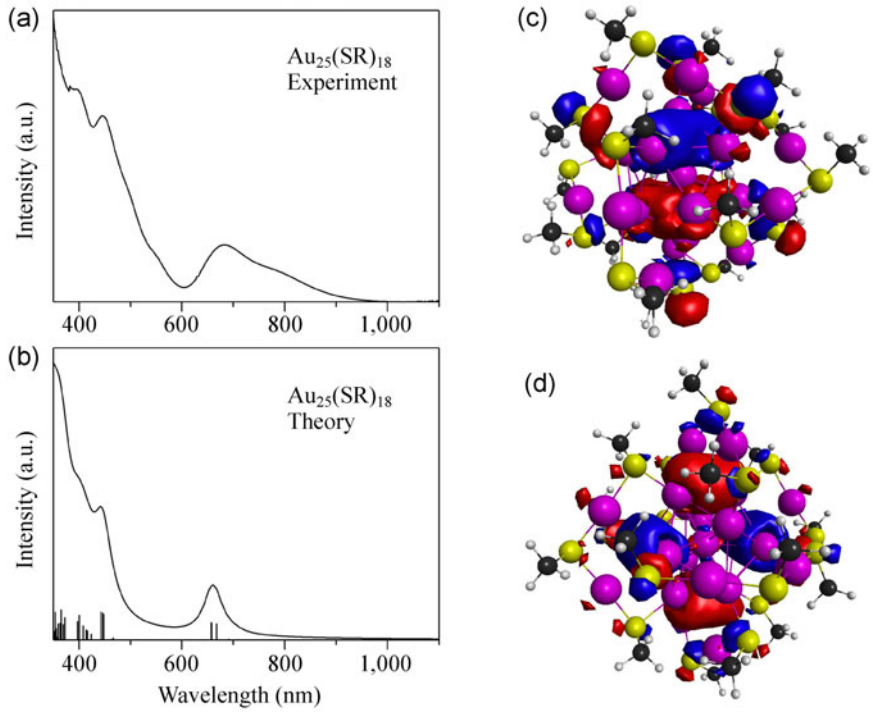

Figure 3 (a) Experimental and (b) TDDFT-simulated spectra of $Au_{25}(SR)_{18}$. (c) HOMO and (d) LUMO of $Au_{25}(SR)_{18}$.

synthetic strategy for bimetal nanoclusters involves co-reduction of gold and heterometal salt precursors. By varying the salt ratios, one can control the Au:heterometal ratio in the final nanocluster product. In regards to the terminology, if a specific number of heteroatom(s) is introduced into the gold cluster, we call it "doping", whereas the case of a distribution of heteroatoms is termed "alloying".

2.1.1 Pd doping

Murray et al. observed by mass spectrometry (MS) a monopalladium-doped $Pd_1Au_{24}(SC_2H_4Ph)_{18}$ species in a product mixed with other species (predominantly $Au_{25}(SC_2H_4Ph)_{18}$) [35]. Interestingly, the $Pd_1Au_{24}(SC_2H_4Ph)_{18}$ composition was obtained irrespective of the starting ratio of Au(III) to Pd(II) salt in the synthesis [35], showing that only one Pd atom can be doped into the 25-atom gold nanocluster. In a theoretical study, Jiang and Dai. predicted that 16 elements from groups 1, 2, and 10–14, including Pd, can be used to replace the central atom of $Au_{25}(SR)_{18}$ while maintaining the electronic and geometric structures [20]. Other theoretical analyses also indicated that the centrally doped $Pd_1Au_{24}(SC_2H_4Ph)_{18}$ structure is the most energetically stable one [21, 36].

Negishi and coworkers first obtained molecular purity $Pd_1Au_{24}(SC_{12}H_{25})_{18}$ nanoclusters via solvent extraction and chromatographic separation to remove the coexisting $Au_{25}(SR)_{18}$ from the synthesis [37]. Qian et al. [38] devised two synthetic protocols for obtaining $Pd_1Au_{24}(SC_2H_4Ph)_{18}$, including a two-phase (water/toluene) synthesis and a one-phase (tetrahydrofuran (THF)) approach based upon previous work [7, 39, 40]). It is worth noting that tetraoctylammonium bromide (TOAB)—the phase transfer agent typically used in the two-phase synthesis—was used even in the one-phase method which in principle does not need TOAB, as it was found that TOAB facilitates the formation and protects the Au_{25} nanoclusters [41]. Pure $Pd_1Au_{24}(SC_2H_4Ph)_{18}$ nanoclusters were isolated by solvent (acetonitrile) extraction and size exclusion chromatography [37, 38]. The formula was deduced based upon the precise cluster mass determined by MS (Fig. 4(b)). Unlike the native $Au_{25}(SR)_{18}$ nanocluster which carries a –1 charge, $Pd_1Au_{24}(SR)_{18}$ was interestingly found to be neutral by various methods [37, 38]. In recent work Negishi et al. [42] further conducted ESI-MS analysis of $Pd_1Au_{24}(SC_{12}H_{25})_{18}$; no ion peak was observed in either positive- or negative-ion mode. On the other hand, when a $Pd_1Au_{24}(SC_{12}H_{25})_{18}$

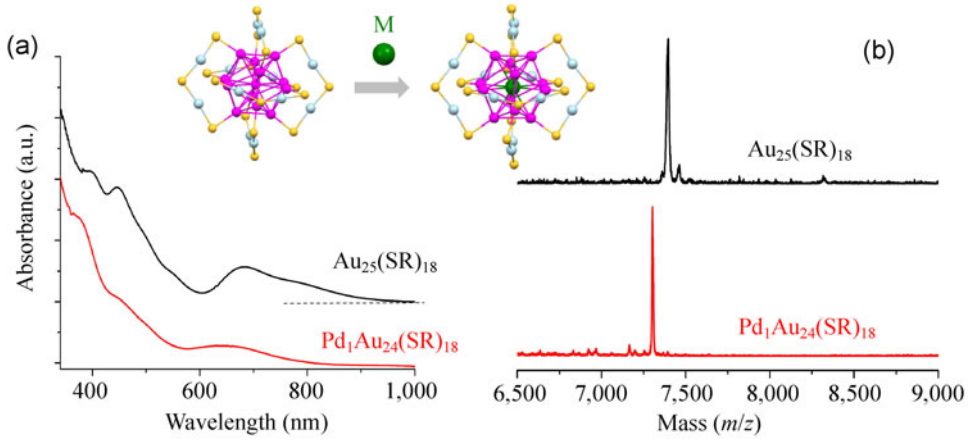

Figure 4 UV–vis absorption spectra (a) and MALDI-MS (b) of $Au_{25}(SR)_{18}$ (black profiles) and $Pd_1Au_{24}(SR)_{18}$ (red profiles). Adapted with permission from Ref. [1], Copyright American Chemical Society 2012.

solution was mixed with a small amount of $[(C_4H_9)_4N]^+[ClO_4]^-$, an ion peak of an adduct of the type $[Pd_1Au_{24}(SC_{12}H_{25})_{18}][N(C_4H_9)_4]^+$ was observed in positive mode ESI-MS analysis, hence, further confirming the neutral state of $Pd_1Au_{24}(SC_{12}H_{25})_{18}$ [42]. The optical spectra of the two clusters show some differences (Fig. 4(a)) and the three bands become less pronounced in $Pd_1Au_{24}(SR)_{18}$ compared with $Au_{25}(SR)_{18}$.

It is interesting that a difference of a single atom between the two clusters can lead to distinct differences in their UV–vis spectra. The optical spectrum is not dependent on the *R* group in the ligand (e.g., R = $C_{12}H_{25}$ or C_2H_4Ph) [37, 38]. Of note, however, the chiroptical signals (e.g., CD) are strongly dependent on the chiral nature of the R groups [43, 44].

There is so far no crystal structure available for the doped nanocluster, thus experimental analysis of the overall structure and the specific location of the dopant atom is indirect. Nevertheless, the $Pd_1Au_{24}(SR)_{18}$ nanocluster was proved to adopt the same structure as that of the homogold $Au_{25}(SR)_{18}$ nanocluster [37, 38]. A particularly interesting question pertains to the exact location of the single Pd atom. On the basis of the $Au_{25}(SR)_{18}$ structure, there are three types of possible doping sites to accommodate the Pd atom: (1) in the center of the icosahedral Au_{13} kernel (Fig. 2, blue atom), (2) in the icosahedral shell (i.e., any one of the magenta sites), and (3) in the exterior Au_{12} shell (i.e., any of the green sites). All experimental and theoretical evidence indicates that the Pd atom is located in the center of $Pd_1Au_{24}(SR)_{18}$. Experimentally, both matrix-assisted laser desorption ionization (MALDI) and laser desorption ionization (LDI) MS fragmentation analyses gave exclusively the $Au_4(SR)_4$ fragment—which results from the exterior surface of the cluster—and this rules out the possibility of Pd being located in the exterior shell [37, 38]. Theoretical analysis of the stability (in terms of energy) found that the centrally doped $Pd_1Au_{24}(SR)_{18}$ is the most stable [20, 21, 36, 37], and the similarity between the simulated spectrum of centrally doped $Pd_1Au_{24}(SR)_{18}$ and the experimental one also confirms the central doping (Figs. 5(a) and 5(b)). Nobusada and coworkers performed DFT calculations on $Pd_1Au_{24}(SR)_{18}$ [37] and found that the optimized structure of the centrally doped $Pd_1Au_{24}(SR)_{18}$ generally resembles the structure of $Au_{25}(SR)_{18}$ except for the slight elongation of the icosahedral $Pd@Au_{12}$ kernel. The TDDFT simulated optical spectrum of the centrally doped $Pd_1Au_{24}(SR)_{18}$ (Fig. 5(b)) is in good accordance with the experimental one (Fig. 5(a)). The first broad hump centered at 650 (experiment), which is reproduced by the simulated peaks at 650–660 nm and at 550–600 nm. These simulated peaks are primarily attributed to a HOMO to LUMO+1 transition (650–660 nm) and to a transition from lower MOs to LUMO (550–600 nm). Figures 5(c)–5(e) show illustrations of HOMO, LUMO and LUMO+1 of $Pd_1Au_{24}(SR)_{18}$. Because both HOMO and LUMO have an atom-like Pd 5p character from the central Pd, the HOMO–LUMO transition is strongly suppressed, i.e., it is almost dipole forbidden transition.

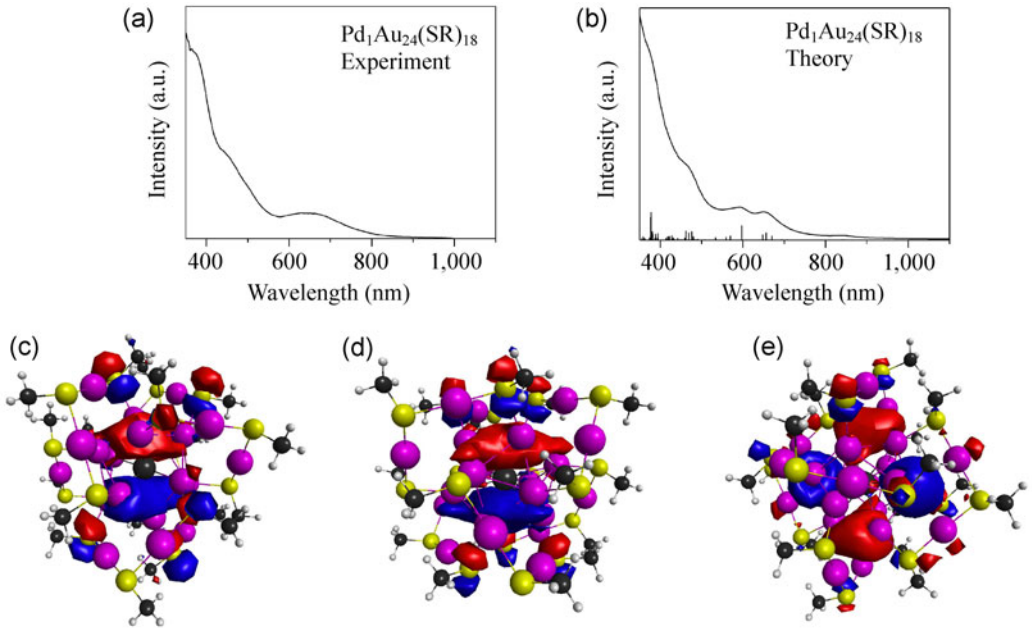

Figure 5 (a) Experimental and (b) TDDFT-simulated spectra of $Pd_1Au_{24}(SR)_{18}$. (c) HOMO, (d) LUMO and (e) LUMO+1 of $Pd_1Au_{24}(SR)_{18}$.

2.1.2 *Pt doping*

Among the dopants Pd, Pt, Ag, and Cu, the platinum-doped $Pt_1Au_{24}(SR)_{18}$ nanocluster was predicted to be the most stable i.e., having the largest interaction energy between the central dopant and the surrounding $Au_{12}/Au_{12}(SR)_{18}$ framework [20]. Experimentally, confirming Pt doping of the 25-atom nanocluster was quite challenging due to the difficulty in discriminating Pt from Au since their atomic masses differ merely by 1.89 Da, which requires high precision ESI-MS analysis. Qian et al. [45] employed a one-phase method (with THF as the solvent) to obtain $Pt_1Au_{24}(SC_2H_4Ph)_{18}$ (mixed with $Au_{25}(SC_2H_4Ph)_{18}$). $Pt_1Au_{24}(SC_2H_4Ph)_{18}$ was isolated from the mixture by size exclusion chromatography. The $Pt_1Au_{24}(SC_2H_4Ph)_{18}$ cluster was found to be very robust in oxidizing environments, which allowed selective decomposition of $Au_{25}(SC_2H_4Ph)_{18}$ by reaction with concentrated H_2O_2 (30 wt.%), and hence, the $Pt_1Au_{24}(SC_2H_4Ph)_{18}$ species was enriched in the crude product prior to isolation by size exclusion chromatography. $Pt_1Au_{24}(SC_2H_4Ph)_{18}$ was charge neutral, similar to $Pd_1Au_{24}(SC_2H_4Ph)_{18}$.

To probe the structure of the nanocluster and the position of the Pt dopant, Qian et al. [45] performed nuclear magnetic resonance (NMR), powder X-ray diffraction (XRD), LDI and MALDI fragmentation analyses. NMR spectroscopy is useful for probing the ligand environment (a manifestation of the symmetry of the metal core). 1D and 2D-correlation NMR analyses of $Pt_1Au_{24}(SC_2H_4Ph)_{18}$ identified two types of ligand environments (in a 2:1 ratio), which is consistent with the ligand distribution pattern in $Au_{25}(SR)_{18}$, implying their similar structure. Indeed, even the ^1H chemical shifts of $Pt_1Au_{24}(SC_2H_4Ph)_{18}$ are similar to those of $Au_{25}(SC_2H_4Ph)_{18}$, which strongly implies that the ligands are bonded to the same type of metal atom (i.e., Au) in both clusters; otherwise, if Pt is located in one of the staples or at the surface of the icosahedron, it would break the high symmetry of the ligand environment and affect the NMR pattern as well as the chemical shifts; this is strong evidence that Pt is located in the central site. DFT calculations were performed to compare the energies of the three isomers of the $Pt_1Au_{24}(SCH_3)_{18}$ cluster. The central doping of Pt is indeed the most stable configuration, followed by doping in the Au_{12} icosahedral shell (35 kJ/mol higher in energy) and then in the staple motif (73 kJ/mol higher in energy) [45].

Unlike the case of Pd doping, $Pt_1Au_{24}(SR)_{18}$ showed a significantly different optical spectrum from that of $Pd_1Au_{24}(SR)_{18}$ or $Au_{25}(SR)_{18}$. A distinct peak in the

visible range was found at 590 nm, with an additional broad peak in the near-infrared (NIR) range centered at ~1,100 nm [45]. The onset of optical absorption of $Pt_1Au_{24}(SR)_{18}$ clusters was determined to be ~0.8 eV (taken as the optical energy gap, obtained by extrapolating the lowest-energy peak to zero absorbance), which is much smaller than that of $Au_{25}(SR)_{18}$ clusters (~1.33 eV). TDDFT calculations by Nobusada showed that the spectrum of centrally doped $Pt_1Au_{24}(SR)_{18}$ matches best with the experimental spectrum (Fig. 6). Interestingly, the HOMO–LUMO transition is forbidden. The experimentally observed peak at 1,100 nm indeed corresponds to the HOMO-2 to LUMO transition. Of note, the HOMO-2 orbital has contributions from all over the cluster. This indicates that the electronic structure of $Pt_1Au_{24}(SCH_3)_{18}$ is more complex than $Au_{25}(SR)_{18}$—which is a result of Pt doping. The simulated peak at 2.2 eV (or 590 nm) involves multiple absorption lines (Fig. 6(b)). The HOMO, LUMO and LUMO+1 of $Pt_1Au_{24}(SR)_{18}$ are shown in Figs. 6(c)–6(e).

MacDonald et al. [46] probed the electronic structure of $Au_{25}(SR)_{18}$ by X-ray absorption spectroscopy. Furthermore, they investigated the Pt-doped nanocluster [47]. Extended X-ray absorption fine structure (EXAFS) spectroscopy is element-specific, which makes it an ideal tool for probing the location of the Pt-dopant via determination of the Pt coordination number (CN). In terms of the three possible sites for Pt, if Pt is in the center then a Pt–Au shell will result, if Pt is in the icosahedral shell then Pt–Au and Pt–S shells will be present, whereas only a Pt–S shell will be present if Pt is in the staple. Christensen et al. [47] used the Pt L3-edge EXAFS (Fig. 7) to deduce the location of the Pt dopant by focusing on Pt–Au CN value for Pt in each possible location—which is dramatically different for the three possible sites. The experimental Pt–Au CN value indeed matches most closely with the central site. Thus, the Pt dopant was clearly determined to be in the center of the cluster. Photoelectron spectroscopic studies of the doped nanocluster shed more light on the complex electronic structure; X-ray photoelectron spectroscopy (XPS) analysis showed a distinct narrowing in the Au 4f peaks of $Pt_1Au_{24}(SR)_{18}$ compared to $Au_{25}(SR)_{18}$, which is ascribed to the contractions in metal–sulfur and metal–metal bond lengths in $Pt_1Au_{24}(SCH_3)_{18}$ [47]. Thus, bimetallic bonding and bond contraction have large effects on the electronic properties of $Pt_1Au_{24}(SCH_3)_{18}$.

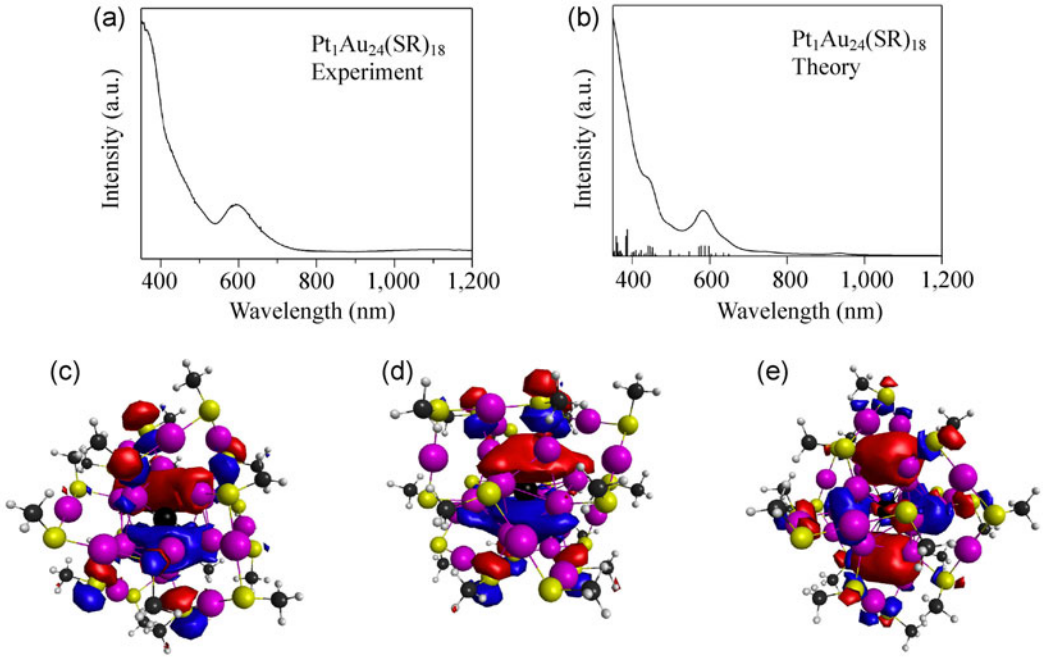

Figure 6 (a) Experimental and (b) TDDFT simulated spectra of $Pt_1Au_{24}(SR)_{18}$. (c) HOMO, (d) LUMO and (e) LUMO+1 of $Pt_1Au_{24}(SR)_{18}$. Note: In Figure 6(a), the broad peak centered at ~1,100 nm is hard to discern due to its broadness on the wavelength scale, but becomes prominent on the photon energy scale [45].

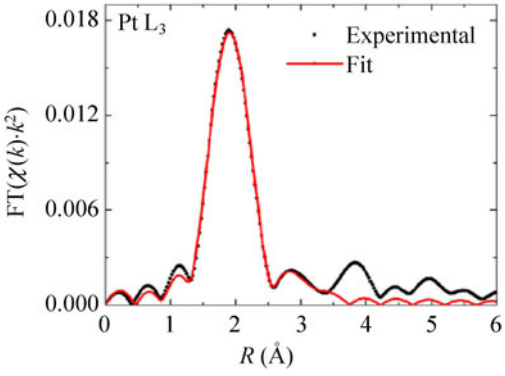

Figure 7 Analysis of the Pt position in the $Pt_1Au_{24}(SR)_{18}$ nanocluster by probing the Pt L3-edge EXAFS. Adapted with permission from Ref. [47], Copyright American Chemical Society 2012.

2.1.3 *Ag alloying*

Unlike the cases of Pd and Pt doping, a distribution of Ag dopants in $Ag_xAu_{25-x}(SR)_{18}$ was found by Negishi et al. [48] following a similar synthetic approach as that used for $Pd_1Au_{24}(SC_{12}H_{25})_{18}$. Various molar ratios of $[HAuCl_4]$:$[AgNO_3]$ were tested, including 22:3, 19:6, 15:10, 10:15, 8:17, and 5:20, and the cluster products, denoted as 1–6, respectively, were extracted from the dried crude products with acetone. TEM analysis of 1–6 confirmed their uniform size (~1 nm), consistent with the expected size of 25-atom clusters; note, however, that TEM does not allow the precise number of atoms to be determined. MALDI-MS analysis in either + or – mode showed a unimodal distribution of $Ag_xAu_{25-x}(SC_{12}H_{25})_{18}$, with both the average number of Ag atoms and the range increasing continuously with increasing $[AgNO_3]$:$[HAuCl_4]$ ratio in the precursor mixture. These results are in striking contrast with the cases of Pd and Pt doping, where only a single Pd or Pt atom could be incorporated into the 25-atom cluster no matter how high the heterometal salt Au(III) ratio was.

By LDI-MS fragmentation analysis, Negishi et al. [48] confirmed that the structure of $Ag_xAu_{25-x}(SC_{12}H_{25})_{18}$ is similar to that of $Au_{25}(SR)_{18}$. They further performed XPS on the sample with the most abundant composition of $Ag_6Au_{19}(SC_{12}H_{25})_{18}$ and found that the Au 4f peak (83.8 eV) is lower in binding energy than that of that of Au(0) (84.0 eV) and $Au_{25}(SC_{12}H_{25})_{18}$ (84.3 eV), implying electron density transfer from Ag to Au atoms in the cluster, that is, $Ag^{\delta+}$ and $Au^{\delta-}$. This is consistent with the relative electronegativities (Ag 1.93 vs. Au 2.54). Work by Gottlieb et al. [49] on Ag doping in $Au_{25}(SCH_2CH_2Ph)_{18}$ found similar results. DFT calculations on monodoped $[Ag_1Au_{24}(SCH_3)_{18}]^q$ ($q = -1, 0, +1$) [22, 36] and on triply doped $[Ag_3Au_{22}(SCH_3)_{18}]^-$ [50] found that the structure with the Ag atom(s) located in the icosahedral shell was more energetically stable than other isomers.

The optical spectrum of $Ag_xAu_{25-x}(SR)_{18}$ was found to be very sensitive to the number of Ag atoms [48, 49]. Generally, the spectrum becomes less featured with increasing Ag doping. A blue shift of optical absorption with increasing number of Ag atoms was observed [48] and this was also modeled theoretically [22]. Photoluminescence measurements revealed that $Ag_xAu_{25-x}(SC_{12}H_{25})_{18}$ exhibits blue shifted emission compared to $Au_{25}(SR)_{18}$ (emission at 1060 nm). These trends are independent of the ligand type (e.g., $SC_{12}H_{25}$ vs. SC_2H_4Ph).

2.1.4 *Cu alloying*

Like Ag, copper is in the same group as gold. The atomic size of Cu (r = 1.28 Å) is much smaller than that of gold (1.44 Å). Unlike the Ag–Au bond, which is weaker than Au–Au, the Cu–Au bond is instead stronger than Au–Au [51]. In the synthesis of Cu-doped clusters [49, 52], similar behavior as that for silver doping was observed (i.e., a continuous distribution, instead of a specific number of dopants). The maximum number of Cu atoms was up to $x = 5$ in $Cu_xAu_{25-x}(SR)_{18}$, much less than the case of Ag (which was up to $x = 11$), with decreasing yield of $Cu_xAu_{25-x}(SR)_{18}$ for higher x. This is indicative of the instability of nanoclusters highly doped by Cu. The smaller size of the copper atom (1.28 Å) is considered to induce significant distortion in the cluster structure, thus causing instability of $Cu_xAu_{25-x}(SR)_{18}$ [52].

Negishi et al. [52] modeled the copper site for the case of a mono-doped $Cu_1Au_{24}(SCH_3)_{18}$ nanocluster. The absorption spectra of the three isomers were calculated, with the single copper atom (1) in the center of the icosahedral core, (2) at the surface of the icosahedron, and (3) in the –SR–Au–SR–Au–SR– staple or oligomer. The absorption spectrum of case-1 shifts to a lower energy relative to that of $[Au_{25}(SCH_3)_{18}]^-$, indicative of a smaller HOMO–LUMO gap, while no change was found in the spectrum for (3), and the

absorption spectrum of (2) shifted to a higher energy relative to $[Au_{25}(SCH_3)_{18}]^-$, indicative of a larger HOMO–LUMO gap. Negishi et al. concluded that the Cu atom in $Cu_1Au_{24}(SR)_{18}$ should occupy the central site due to its atomic size being smaller than Ag and Au (that is, Cu is more easily trapped in the center), although configuration (2) is actually energetically more stable. With increasing number of Cu dopant atoms, the Cu atoms are incorporated in the icosahedral shell.

On the other hand, DFT analysis [52] indicated that the geometric structure of the $Cu_1Au_{24}(SCH_3)_{18}$ cluster was significantly distorted regardless of the copper location. In contrast, silver doping barely distorts the structure no matter where the Ag atom was located, due to the comparable sizes of Ag and Au. This major difference might account for their differences in stability and suggests that the dopant should be of very similar atomic radius to that of gold in order to maintain the stability of the nanocluster [52].

2.2 The case of 38-gold atom (Au_{38}) nanoparticles

The Tsukuda group unequivocally determined the formula of $Au_{38}(SC_{12}H_{25})_{24}$ by ESI-MS [53]. Qian et al. developed a size-focusing method and obtained molecular purity $Au_{38}(SR)_{24}$ nanoclusters [54] and further succeeded in the growth of single crystals of $Au_{38}(SCH_2CH_2Ph)_{24}$ [55]. The total structure was solved by X-ray crystallography. The $Au_{38}(SCH_2CH_2Ph)_{24}$ nanocluster comprises a face-sharing biicosahedral Au_{23} kernel (Fig. 8(a)), and the kernel is protected by three monomeric staples and six dimeric staples (Fig. 8(b)) [55]. The cluster is chiral and two enantiomers coexist in the unit cell. The optical spectrum contains a number of bands at 400, 478, 517, 630, 750, 1,050 nm, with the latter three being very distinct (Fig. 9) [53, 54]. The 1,050 nm band was shown to be the HOMO–LUMO transition [56, 57], with a band gap of 0.9 eV [53–57], consistent with electrochemical measurements [58]. The chirality [59, 60] and cryogenic optical absorption [61] of $Au_{38}(SR)_{24}$ have also been studied.

2.2.1 *Pd doping*

With respect to Pd doping in $Au_{38}(SR)_{24}$, if the palladium atom occupies the center of the icosahedron, then there are two possible cases: mono- and bi-doped

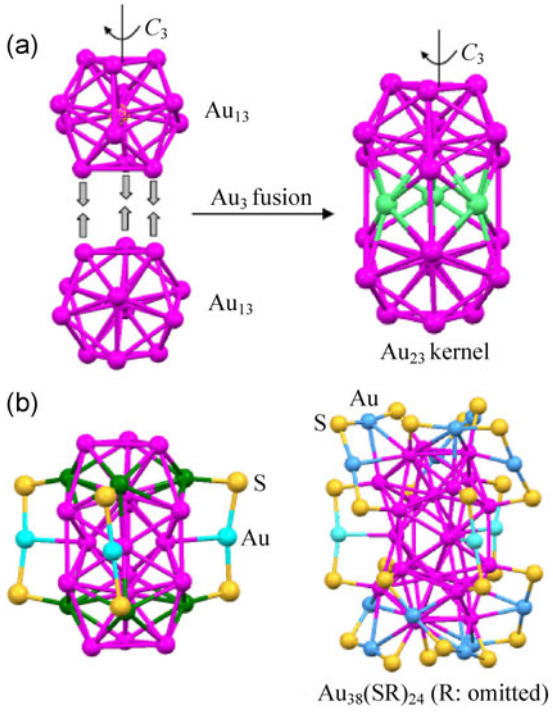

Figure 8 Structure of $Au_{38}(SR)_{24}$ nanoparticles. Adapted with permission from Ref. [55], Copyright American Chemical Society 2010.

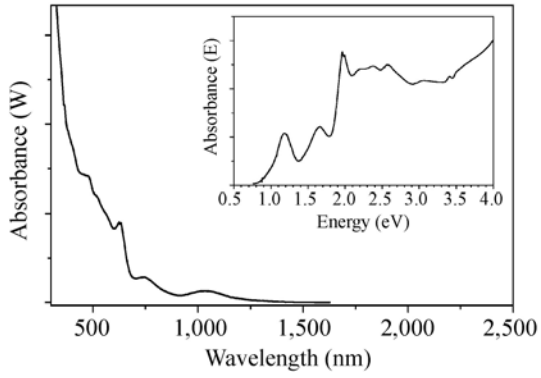

Figure 9 Optical spectrum of $Au_{38}(SR)_{24}$ nanoclusters. Adapted with permission from Ref. [54], Copyright American Chemical Society 2009.

clusters. Qian et al. [38] indeed observed both clusters, $Pd_1Au_{37}(SR)_{24}$ and $Pd_2Au_{36}(SR)_{24}$, but no pure clusters were obtained. In the work by Negishi et al. [62], the $Pd_2Au_{36}(SC_2H_4Ph)_{24}$ was successfully isolated from a mixture which was produced by a one-phase synthesis in THF using $HAuCl_4$ and Na_2PdCl_4 as salt precursors. In the separation steps, $Pd_nAu_{38-n}(SC_2H_4Ph)_{24}$ (n = 1, 2) were first separated from the mixture by removal of most $Pd_nAu_{25-n}(SC_2H_4Ph)_{18}$ (n = 0, 1) clusters with acetonitrile. The as-obtained $Pd_nAu_{38-n}(SC_2H_4Ph)_{24}$

clusters still contained some $Pd_nAu_{25-n}(SC_2H_4Ph)_{18}$ (n = 0, 1) and larger $(Pd–Au)_x$:SC_2H_4Ph clusters. Using recycling size exclusion chromatography, $Pd_nAu_{38-n}(SC_2H_4Ph)_{24}$ (n = 1, 2) were isolated. Next, by utilizing the higher stability of $Pd_2Au_{36}(SC_2H_4Ph)_{24}$ relative to that of $Pd_1Au_{37}(SC_2H_4Ph)_{24}$, the latter was selectively decomposed by thermal treatment at 60 °C in THF for 8 days. Pure $Pd_2Au_{36}(SC_2H_4Ph)_{24}$ clusters were obtained (MW = 10,597.0), evidenced by clean MALDI-MS spectra in either – or + mode [62]. The optical spectrum is less featured than that of $Au_{38}(SR)_{24}$. Interestingly, in high-resolution ESI-MS analysis, dianionic $[Pd_2Au_{36}(SC_2H_4Ph)_{24}]^{2-}$ was observed, as opposed to the monocharged cluster observed in MALDI-MS analysis. XPS analysis further confirmed the presence of Pd in the doped gold nanocluster [62].

The preservation of metal atom number (i.e., 38 atoms) suggests that the original structure of $Au_{38}(SR)_{24}$ should be preserved in $Pd_2Au_{36}(SC_2H_4Ph)_{24}$. DFT calculations of $Pd_2Au_{36}(SCH_3)_{24}$ indeed showed that the parent structure is energetically favored [62]. Experimentally, it was found that the $Pd_2Au_{36}(SC_2H_4Ph)_{24}$ cluster exhibits higher stability than $Au_{38}(SR)_{24}$ against degradation in solution as well as core etching by thiols [62]. In stability tests, a THF solution of a mixture of $Pd_2Au_{36}(SC_2H_4Ph)_{24}$, $Pd_1Au_{37}(SC_2H_4Ph)_{24}$, and $Au_{38}(SC_2H_4Ph)_{24}$ was subjected to thermal treatment at 60 °C under stirring. After 10 days, only $Pd_2Au_{36}(SC_2H_4Ph)_2$ survived. In tests of the stability of $Pd_2Au_{36}(SC_2H_4Ph)_2$ against core etching by thiols, the mixture was incubated in neat PhC_2H_4SH and heated to 80 °C; after 12 hours, only $Pd_2Au_{36}(SC_2H_4Ph)_2$ was left in the solution. Similar to the higher stability of $Pd_1Au_{24}(SR)_{18}$ relative to $Au_{25}(SR)_{18}$, the enhanced stability of $Pd_2Au_{36}(SC_2H_4Ph)_2$ can be attributed to the higher interaction energy between the two central Pd atoms and the surrounding gold cage. It is worth noting, however, that $Pd_1Au_{37}(SC_2H_4Ph)_{24}$ (charge state –1 by ESI-MS) did not exhibit higher stability than $Au_{38}(SC_2H_4Ph)_{24}$, and indeed was somewhat less stable than $Au_{38}(SC_2H_4Ph)_{24}$. The asymmetry (i.e., only one center is Pd-doped while the other center is still Au) could be a reason [62], but deeper insight is still needed.

The –1 charge state of $Pd_1Au_{37}(SC_2H_4Ph)_{24}$ and –2 of $Pd_2Au_{36}(SC_2H_4Ph)_{24}$ are in contrast to the neutral $Pd_1Au_{24}(SR)_{18}$. More work is still needed to account for their differences in charge state and trends in stability. Of note, no work on Pt substitution in $Au_{38}(SR)_{24}$ has been done, and this would be worth carrying out in future work.

2.2.2 *Ag alloying*

Dass and coworkers [63] carried out Ag doping in $Au_{38}(SR)_{24}$ and observed continuous Ag substitution, in contrast with the discrete substitution by one or two Pd atoms. With increasing silver content in the salt precursors, the number of silver atoms in the final cluster product increases as expected. A plateau was observed at 1:0.20 Au(III):Ag(I) molar ratio in the salt precursors, with the most abundant peak of Ag = 6 for a Au(III):Ag(I) ratio of 1:0.20, and the maximum number of Ag = 10 for the Au(III):Ag(I) ratio of 1:0.30. With higher Ag contents in the synthesis mixture, e.g., 1:0.35 and 1:0.40, the yield of clusters dropped significantly and only a minor amount of $Ag_xAu_{38-x}(SR)_{24}$ was obtained with x up to 12, with the most abundant species being Ag = 9. With even higher Ag contents in the synthesis mixture (e.g., beyond 1:0.40), no $Ag_xAu_{38-x}(SR)_{24}$ was detected by mass spectrometric analysis, indicating the instability of the products or the difficultly in the formation of such products [63].

Similar to the case of Ag-doping in $Au_{25}(SR)_{18}$, the optical peaks of $Ag_xAu_{38-x}(SR)_{24}$ were found to be quite sensitive to the number of silver atoms incorporated. Specifically, silver substitution of Au atoms in the cluster leads to a blue shift in the absorption peaks and diminishment of the intensity of optical peaks. With respect to the Ag dopant positions, based on the $Au_{38}(SR)_{24}$ structure, several possibilities for silver atoms exist as follows: (1) silver atoms in the staples exclusively (note: the staples can take up to 15 metal atoms); (2) in both the staples and the Au_{23} kernel; and (3) exclusively in the 23-atom kernel. Dass et al. ruled out option 1, as it cannot explain the diminishing intensity of the optical peaks. In option 3, silver atoms may be distributed between the two face-sharing Ag_nAu_{13-n} icosahedrons (up to an average of 6, and a maximum of 10 for the stable Ag_nAu_{23-n} kernel) [63].

Overall, the stability of $Ag_xAu_{38-x}(SR)_{24}$ seems less than $Au_{38}(SR)_{24}$, especially for the highly doped

$Ag_xAu_{38-x}(SR)_{24}$ species. For example, Dass et al. found that, at Au(III):Ag(I) ratios beyond 1:0.30, only minor quantities of $Ag_xAu_{38-x}(SR)_{24}$ ($6 \leqslant x \leqslant 12$) could be observed in the initial stages of etching and such highly doped species were found to decompose over time. The metal–metal bond strength variation was invoked to explain the stability [63]. In bulk Au–Ag alloys, the metal–metal bond strength was found to be Au–Au > Au–Ag > Ag–Ag [64]. Thus, increasing the number of silver atoms would generate more Au–Ag and Ag–Ag bonds, which are weaker than Au–Au bonds, resulting in the lower stability of $Ag_xAu_{38-x}(SR)_{24}$.

2.3 The case of 144-gold atom (Au_{144}) nanoparticles

Qian Jin [65] obtained molecular purity Au_{144} nanoclusters in high yield and unequivocally determined the formula $Au_{144}(SR)_{60}$ by high precision ESI-MS analysis (Figs. 10(a)–10(c)) in conjunction with other characterization methods. It should be noted that in earlier work by Tsukuda group [53], a formula of $Au_{144}(SR)_{59}$ was reported; the one-ligand discrepancy was probably caused by the oxidation treatment of Au_{144} nanoclusters prior to ESI-MS analysis in the work of Tsukuda et al., while in Qian's work the Au_{144} particles were imparted with charges by formation of adduct with Cs^+, which is benign, rather than the destructive oxidation treatment. The atomic structure has not been solved thus far. The optical spectrum of $Au_{144}(SR)_{60}$ is independent of the types of thiolates [53, 65, 66] and shows less pronounced bands compared to $Au_{25}(SR)_{18}$ and $Au_{38}(SR)_{24}$, but two bands can be observed at 505 and 675 nm (Fig. 10(d)).

With respect to heteroatom substitution, Dass et al. [67] performed Ag alloying and observed a distribution of $Ag_xAu_{144-x}(SR)_{60}$ species. The total number of metal atoms (i.e., 144) is retained, similar to the $Ag_xAu_{25-x}(SR)_{18}$ and $Ag_xAu_{38-x}(SR)_{24}$ cases. By measuring the precise cluster weight by ESI-MS (e.g., using the 3– ion set), the number of incorporated Ag atoms were deduced. For each Au(III) to Ag(I) precursor ratio employed, a distribution of $Ag_xAu_{144-x}(SR)_{60}$ was found, rather than a specific number of Ag atoms. Generally, with increasing Ag contents in the Au(III):Ag(I) precursor mixtures, the number of incorporated Ag atoms increases. Their experiments showed that higher Ag(I)

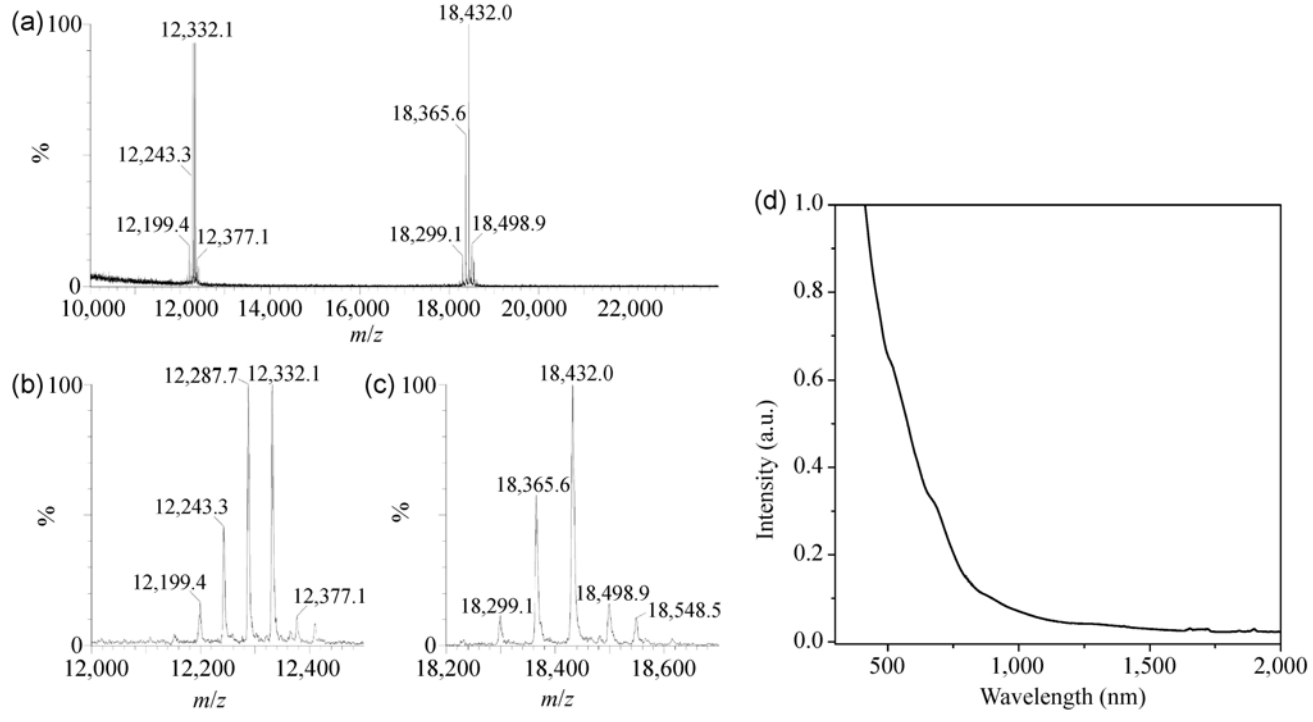

Figure 10 $Au_{144}(SR)_{60}$ nanoclusters: (a)–(c) ESI-MS analysis of the cluster composition; (d) the optical spectrum. Adapted with permission from [65], Copyright American Chemical Society 2009.

contents than Au(III):Ag(I) = 1:1 did not lead to stable $Ag_xAu_{144-x}(SR)_{60}$ alloy nanoclusters.

Unlike the case of $Ag_xAu_{38-x}(SR)_{24}$ in which the spectral peaks diminish with increasing Ag incorporation, the $Ag_xAu_{144-x}(SR)_{60}$ spectra became instead more distinct after Ag doping: for example, $Ag_xAu_{144-x}(SR)_{60}$ exhibits a pronounced peak at 425 nm and shoulder bands at 310 and 560 nm. The $Ag_xAu_{144-x}(SR)_{60}$ alloy nanoclusters can also be synthesized using various types of thiols other than phenylethanethiol, including dodecanethiol and hexanethiol. The optical spectra of the resulting clusters are identical. The opposite trends for $Ag_xAu_{38-x}(SR)_{24}$ and $Ag_xAu_{144-x}(SR)_{60}$ are interesting and remain to be understood after the total structure of $Au_{144}(SR)_{60}$ is solved and the positions of Ag dopants are located in future work. The difference could be caused by the difference in Ag positions and/or the overall electronic structures of these two systems. The bandgaps of $Ag_xAu_{144-x}(SR)_{60}$ have been measured [68] and the electronic structure of alloyed clusters has been analyzed theoretically [69].

2.4 Catalytic application of doped nanoclusters

Herein we briefly comment on the effect of doping on the catalytic properties of nanoclusters. The catalytic activity of $Pd_1Au_{24}(SR)_{18}$ supported on carbon nanotubes (CNT) was evaluated in the oxidation of benzyl alcohol [70]. The ligand-removed Pd_1Au_{24}/CNT catalyst was found to significantly enhance the catalytic activity (74% conversion of $PhCH_2OH$, compared to 22% over undoped Au_{25}/CNT). The effect of the single-Pd-atom was ascribed to the modulation of the electronic structure of the cluster by electron transfer from Pd to Au. In the case of $Pt_1Au_{25}(SR)_{18}$, the supported cluster on TiO_2 was also found to exhibit much higher activity than the undoped cluster in the selective oxidation of styrene with $PhI(OAc)_2$ as the oxidant [45]: a 90.8% conversion of styrene was obtained with the doped cluster catalyst compared to 58.9% over the undoped $Au_{25}(SR)_{18}/TiO_2$ catalyst, and the selectivity for benzaldehyde (89.9%) was also higher than that over the $Au_{25}(SR)_{18}/TiO_2$ catalyst (54.0%). These examples are remarkable and demonstrate the possibility of tuning the catalytic properties of nanoclusters by unprecedented single-atom doping.

3 Conclusions

Ultrasmall gold nanoparticles (i.e., quantum-sized nanoclusters), as well as the doped/alloyed nanoparticles, exhibit unique atom-packing and interesting properties such as the discrete electronic structures, single-electron transitions in optical absorption, and remarkable catalytic properties. In terms of substitution behavior, two scenarios have generally been found: (1) a specific number of heteroatoms being incorporated into the gold nanocluster irrespective of the salt precursor ratios (e.g., Pd or Pt doping), and (2) a distribution of heteroatoms that depends on the initial salt ratio (e.g., Ag or Cu doping). In the latter case, pure $Ag_xAu_{25-x}(SR)_{18}$ or $Ag_xAu_{38-x}(SR)_{24}$ clusters with a specific value of x have not been isolated, and it would be highly interesting if specific isomers could be separated in future work. Pd- or Pt-doped nanoclusters are generally more stable than homogold nanoclusters, while Ag or Cu doped ones are somewhat less stable, especially in the case of Cu-doped nanoclusters. Negishi et al. recently found that using selenolate (as opposed to thiolate) as the ligand, the $Cu_xAu_{25-x}(SeC_8H_{17})_{18}$ clusters indeed become much more stable, and also more Cu atoms (up to 9) can be doped into the 25-atom cluster [71]. These results imply that the role of ligands in cluster stability should be fully taken into consideration.

The optical spectra of $Au_{25}(SR)_{18}$, $Au_{38}(SR)_{24}$ and $Au_{144}(SR)_{60}$ are very sensitive to the type and number of dopant atoms, indicating that the electronic structure can be modulated by incorporating heterometal atoms into the gold core. Overall, a remarkable feature is that the structures of homogold nanoclusters are demonstrated to be very robust, as the doped nanoclusters adopt the original metal-atom framework, though in some cases (e.g., Cu doping) structural distortion was found in DFT simulations. This result suggests that the atomic packing structures largely account for the extraordinary stability of the nanoclusters. Doping with foreign atoms allows researchers to probe the perturbation effects on the properties of nanoclusters. The effect of doping on other properties such as circular dichroism [43, 60, 72] is worth investigating in future work.

On the other hand, the larger counterparts of

nanoclusters—metallic or plasmonic nanoparticles—are still tough to study. In future work, research on both quantum-sized nanoclusters and plasmonic nanoparticles with atomic precision will unravel the nature of particle surface structure, ligand binding modes, and many other fundamental issues. Such knowledge will not only significantly promote basic science but also promote the wide applications of nanoparticles and assembled materials.

Acknowledgements

R. J. acknowledges support by supported by the U.S. Department of Energy—Office of Basic Energy Sciences, grant DE-FG02-12ER16354. K. N. acknowledges support by Grant in Aid (No. 21350018), MEXT, and by the MEXT program "Elements Strategy Initiative to Form Core Research Center" (since 2012). The computation was also partly performed at the Research Center for Computational Science, Okazaki, Japan.

References

[1] Qian, H.; Zhu, M.; Wu, Z.; Jin, R. Quantum sized gold nanoclusters with atomic precision. *Acc. Chem. Res.* **2012**, *45*, 1470–1479.

[2] Jin, R.; Qian, H.; Wu, Z.; Zhu, Y.; Zhu, M.; Mohanty, A.; Garg, N. Size focusing: A methodology for synthesizing atomically precise gold nanoclusters. *J. Phys. Chem. Lett.* **2010**, *1*, 2903–2910.

[3] Maity, P.; Xie, S.; Yamauchiab, M.; Tsukuda, T. Stabilized gold clusters: From isolation toward controlled synthesis. *Nanoscale* **2012**, *4*, 4027–4037 and references therein.

[4] Jin, R. Quantum-sized thiolate protected gold nanoclusters. *Nanoscale* **2010**, *2*, 343–362 and references therein.

[5] Negishi, Y.; Nobusada, K.; Tsukuda, T. Glutathione-protected gold clusters revisited: Bridging the gap between gold(I)–thiolate complexes and thiolate-protected gold nanocrystals. *J. Am. Chem. Soc.* **2005**, *127*, 5261–5270.

[6] Tracy, J. B.; Kalyuzhny, G.; Crowe, M. C.; Balasubramanian, R.; Choi, J.-P.; Murray, R. W. Poly(ethylene glycol) ligands for high-resolution nanoparticle mass spectrometry. *J. Am. Chem. Soc.* **2007**, *129*, 6706–6707.

[7] Zhu, M.; Lanni, E.; Garg, N.; Bier, M. E.; Jin, R. Kinetically controlled, high-yield synthesis of Au_{25} clusters. *J. Am. Chem. Soc.* **2008**, *130*, 1138–1139.

[8] Nimmala, P. R.; Dass, A. $Au_{36}(SPh)_{23}$ nanomolecules. *J. Am. Chem. Soc.* **2011**, *133*, 9175–9177.

[9] Zeng, C.; Qian, H.; Li, T.; Li, G.; Rosi, N. L.; Yoon, B.; Barnett, R. N.; Whetten, R. L.; Landman, U.; Jin, R. Total structure and electronic properties of the gold nanocrystal $Au_{36}(SR)_{24}$. *Angew. Chem. Int. Ed.* **2012**, *51*, 13114–13118.

[10] Qian, H.; Zhu, Y.; Jin, R. Atomically precise gold nanocrystal molecules with surface plasmon resonance. *Proc. Natl. Acad. Sci. USA* **2012**, *109*, 696–700.

[11] Rosi, N. L.; Mirkin, C. A. Nanostructures in biodiagnostics. *Chem. Rev.* **2005**, *105*, 1547–1562.

[12] Garg, N.; Mohanty, A.; Lazarus, N.; Schultz, L.; Rozzi, T. R.; Santhanam, S.; Weiss, L.; Snyder, J. L.; Fedder, G. K.; Jin, R. Robust gold nanoparticles stabilized by trithiol for application in chemiresistive sensors. *Nanotechnology* **2010**, *21*, 405501.

[13] Liu, Y.; Tsunoyama, H.; Akita, T.; Tsukuda, T. Efficient and selective epoxidation of styrene with TBHP catalyzed by Au_{25} clusters on hydroxyapatite. *Chem. Commun.* **2010**, *46*, 550–552.

[14] Li, G.; Jin, R. Atomically precise gold nanoclusters as new model catalysts. *Acc. Chem. Res.* **2013**, *46*, 1749–1758.

[15] Jin, R.; Cao, Y. W.; Hao, E.; Metraux, G. S.; Schatz, G. C.; Mirkin, C. A. Controlling anisotropic nanoparticle growth through plasmon excitation. *Nature* **2003**, *425*, 487–490.

[16] Schaaff, T. G.; Knight, G.; Shafigullin, M. N.; Borkman, R. F.; Whetten, R. L. Isolation and selected properties of a 10.4 kDa gold:glutathione cluster compound. *J. Phys. Chem. B* **1998**, *102*, 10643–10646.

[17] Wyrwas, R. B.; Alvarez, M. M.; Khoury, J. T.; Price, R. C.; Schaaff, T. G.; Whetten, R. L. The colours of nanometric gold: Optical response functions of selected gold-cluster thiolates. *Eur. Phys. J. D* **2007**, *43*, 91–95.

[18] Nobusada, K.; Iwasa, T. Oligomeric gold clusters with vertex-sharing bi- and triicosahedral structures. *J. Phys. Chem. C* **2007**, *111*, 14279–14282.

[19] Pei, Y.; Zeng, X. C. Investigating the structural evolution of thiolate protected gold clusters from first-principles. *Nanoscale* **2012**, *4*, 4054–4072 and references therein.

[20] Jiang, D.; Dai, S. From superatomic $Au_{25}(SR)_{18}$ to superatomic $M@Au_{24}(SR)_{18}$ shell clusters. *Inorg. Chem.* **2009**, *48*, 2720–2722.

[21] Kacprzak, K. A.; Lehtovaara, L.; Akola, J.; Lopez-Acevedoa, O.; Hakkinen, H. A density functional investigation of thiolate-protected bimetal $PdAu_{24}(SR)_{18}^{z}$ clusters: Doping the superatom complex. *Phys. Chem. Chem. Phys.* **2009**, *11*, 7123–7129.

[22] Guidez, E. B.; Mäkinen, V.; Häkkinen, H.; Aikens, C. M. Effects of silver doping on the geometric and electronic structure and optical absorption spectra of the $Au_{25-n}Ag_n(SH)_{18}^{-}$

(n = 1, 2, 4, 6, 8, 10, 12) bimetallic nanoclusters. *J. Phys. Chem. C* **2012**, *116*, 20617–20624.

[23] Sánchez-Castillo, A.; Noguez, C.; Garzón, I. L. On the origin of the optical activity displayed by chiral-ligand-protected metallic nanoclusters. *J. Am. Chem. Soc.* **2010**, *132*, 1504–1505.

[24] Mie, G. Beiträge zur Optik trüber Medien, speziell kolloidaler Metallösungen. *Ann. Phys.* **1908**, *25*, 377–445.

[25] Kreibig, U.; Vollmer, M. *Optical Properties of Metal Clusters*. Springer-Verlag: New York, 1995.

[26] Donkers, R. L.; Lee, D.; Murray, R. W. Synthesis and isolation of the molecule-like cluster $Au_{38}(PhCH_2CH_2S)_{24}$. *Langmuir* **2004**, *20*, 1945–1952.

[27] Heaven, M. W.; Dass, A.; White, P. S.; Holt, K. M.; Murray, R. W. Crystal structure of the gold nanoparticle $[N(C_8H_{17})_4][Au_{25}(SCH_2CH_2Ph)_{18}]$. *J. Am. Chem. Soc.* **2008**, *130*, 3754–3755.

[28] Zhu, M.; Aikens, C. M.; Hollander, F. J.; Schatz, G. C.; Jin, R. Correlating the crystal structure of a thiol-protected Au_{25} cluster and optical properties. *J. Am. Chem. Soc.* **2008**, *130*, 5883–5885.

[29] Wu, Z.; Gayathri, C.; Gil, R.; Jin, R. Probing the structure and charge state of glutathione-capped $Au_{25}(SG)_{18}$ clusters by NMR and mass spectrometry. *J. Am. Chem. Soc.* **2009**, *131*, 6535–6542.

[30] Venzo, A.; Antonello, S.; Gascon, J. A.; Guryanov, I.; Leapman, R. D.; Perera, N. V.; Sousa, A. A.; Zamuner, M.; Zanella, A.; Maran, F. Effect of the charge state (z = –1, 0, +1) on the nuclear magnetic resonance of monodisperse $Au_{25}[S(CH_2)_2Ph]^{z}_{18}$ clusters. *Anal. Chem.* **2011**, *83*, 6355–6362.

[31] Liu, Z.; Zhu, M.; Meng, X.; Xu, G.; Jin, R. Electron transfer between $Au_{25}(SC_2H_4Ph)^{-}_{18}TOA^{+}$ nanoclusters and oxoammonium cations. *J. Phys. Chem. Lett.* **2011**, *2*, 2104–2109.

[32] Aikens, C. M. Electronic Structure of ligand-passivated gold and silver nanoclusters. *J. Phys. Chem. Lett.* **2011**, *2*, 99–104.

[33] Zhu, M.; Eckenhoff, W. T.; Pintauer, T.; Jin, R. Conversion of anionic $[Au_{25}(SCH_2CH_2Ph)_{18}]^{-}$ cluster to charge neutral cluster via air oxidation. *J. Phys. Chem. C* **2008**, *112*, 14221–14224.

[34] Zhu, M.; Aikens, C. M.; Hendrich, M. P.; Gupta, R.; Qian, H.; Schatz, G. C.; Jin, R. Reversible switching of magnetism in thiolate-protected Au_{25} superatoms. *J. Am. Chem. Soc.* **2009**, *131*, 2490–2492.

[35] Fields-Zinna, C. A.; Crowe, M. C.; Dass, A.; Weaver, J. E. F.; Murray, R. W. Mass spectrometry of small bimetal monolayer-protected clusters. *Langmuir* **2009**, *25*, 7704–7710.

[36] Walter, M.; Moseler, M. Ligand-protected gold alloy clusters: Doping the superatom. *J. Phys. Chem. C* **2009**, *113*, 15834–15837.

[37] Negishi, Y.; Kurashige,W.; Niihori, Y.; Iwasa, T.; Nobusada, K. Isolation, structure, and stability of a dodecanethiolate-protected Pd_1Au_{24} cluster. *Phys. Chem. Chem. Phys.* **2010**, *12*, 6219–6225.

[38] Qian, H.; Barry, E.; Zhu, Y.; Jin, R. Doping 25-atom and 38-atom gold nanoclusters with palladium. *Acta Phys. –Chim. Sin.* **2011**, *27*, 513–519.

[39] Wu, Z.; Suhan, J.; Jin, R. One-pot synthesis of atomically monodisperse, thiol-functionalized Au_{25} nanoclusters. *J. Mater. Chem.* **2009**, *19*, 622–626.

[40] Parker, J. F.; Weaver, J. E. F.; McCallum, F.; Fields-Zinna, C. A.; Murray, R. W. Synthesis of monodisperse $[Oct_4N^{+}][Au_{25}(SR)^{-}_{18}]$ nanoparticles, with some mechanistic observations. *Langmuir* **2010**, *26*, 13650–13654.

[41] Zhu, M.; Chan, G.; Qian, H.; Jin, R. Unexpected reactivity of $Au_{25}(SCH_2CH_2Ph)_{18}$ nanoclusters with salts. *Nanoscale* **2011**, *3*, 1703–1707.

[42] Niihori, Y.; Kurashige, W.; Matsuzaki, M.; Negishi, Y. Remarkable enhancement in ligand-exchange reactivity of thiolate-protected Au_{25} nanoclusters by single Pd atom doping. *Nanoscale* **2013**, *5*, 508–512.

[43] Zhu, M.; Qian, H.; Meng, X.; Jin, S.; Wu, Z.; Jin, R. Chiral Au_{25} nanospheres and nanorods: Synthesis and insight into the origin of chirality. *Nano Lett.* **2011**, *11*, 3963–3969.

[44] Kumar, S.; Jin, R. Water-soluble $Au_{25}(Capt)_{18}$ nanoclusters: Synthesis, thermal stability, and optical properties. *Nanoscale* **2012**, *4*, 4222–4227.

[45] Qian, H.; Jiang, D.-E.; Li, G.; Gayathri, C.; Das, A.; Gil, R. R.; Jin, R. Monoplatinum doping of gold nanoclusters and catalytic application. *J. Am. Chem. Soc.* **2012**, *134*, 16159–16162.

[46] MacDonald, M. A.; Chevrier, D. M.; Zhang, P.; Qian, H.; Jin, R. The structure and bonding of $Au_{25}(SR)_{18}$ nanoclusters from EXAFS: The interplay of metallic and molecular behavior. *J. Phys. Chem. C* **2011**, *115*, 15282–15287.

[47] Christensen, S. L.; MacDonald, M. A.; Chatt, A.; Zhang, P.; Qian, H.; Jin, R. Dopant location, local structure, and electronic properties of $Au_{24}Pt(SR)_{18}$ nanoclusters. *J. Phys. Chem. C* **2012**, *116*, 26932–26937.

[48] Negishi, Y.; Iwai, T.; Ide, M. Continuous modulation of electronic structure of stable thiolate-protected Au_{25} cluster by Ag doping. *Chem. Commun.* **2010**, *46*, 4713–4715.

[49] Gottlieb, E.; Qian, H.; Jin, R. Atomic-level alloying and de-alloying in doped gold nanoparticles. *Chem. Eur. J.* **2013**, *19*, 4238–4243.

[50] Kauffman, D. R.; Alfonso, D.; Matranga, C.; Qian, H.; Jin, R. A quantum alloy: The ligand-protected $Au_{25-x}Ag_x(SR)_{18}$ cluster. *J. Phys. Chem. C* **2013**, *117*, 7914–7923.

[51] Ackerman, M.; Stafford, F. E.; Drowart, J. Mass spectrometric determination of the dissociation energies of the molecules

AgAu, AgCu, and AuCu. *J. Chem. Phys.* **1960**, *33*, 1784–1789.

[52] Negishi, Y.; Munakata, K.; Ohgake, W.; Nobusada, K. Effect of copper doping on electronic structure, geometric structure, and stability of thiolate-protected Au_{25} nanoclusters. *J. Phys. Chem. Lett.* **2012**, *3*, 2209–2214.

[53] Chaki, N. K.; Negishi, Y.; Tsunoyama, H.; Shichibu, Y.; Tsukuda, T. Ubiquitous 8 and 29 kDa gold:alkanethiolate cluster compounds: Mass-spectrometric determination of molecular formulas and structural implications. *J. Am. Chem. Soc.* **2008**, *130*, 8608–8610.

[54] Qian, H.; Zhu, Y.; Jin, R. Size-focusing synthesis, optical and electrochemical properties of monodisperse $Au_{38}(SC_2H_4Ph)_{24}$ nanoclusters. *ACS Nano* **2009**, *3*, 3795–3803.

[55] Qian, H.; Eckenhoff, W. T.; Zhu, Y.; Pintauer, T.; Jin, R. Total structure determination of thiolate-protected Au_{38} nanoparticles. *J. Am. Chem. Soc.* **2010**, *132*, 8280–8281.

[56] Pei, Y.; Gao, Y.; Zeng, X. C. Structural prediction of thiolate-protected Au_{38}: A face-fused bi-icosahedral Au core. *J. Am. Chem. Soc.* **2008**, *130*, 7830–7832.

[57] Lopez-Acevedo, O.; Tsunoyama, H.; Tsukuda, T.; Häkkinen, H.; Aikens, C. M. Chirality and electronic structure of the thiolate-protected Au_{38} nanocluster. *J. Am. Chem. Soc.* **2010**, *132*, 8210–8218.

[58] Toikkanen, O.; Carlsson, S.; Dass, A.; Rönnholm, G.; Kalkkinen, N.; Quinn, B. M. Solvent-dependent stability of monolayer-protected Au_{38} clusters. *J. Phys. Chem. Lett.* **2010**, *1*, 32–37.

[59] Qian, H.; Zhu, M.; Gayathri, C.; Gil, R. R.; Jin, R. Chirality in gold nanoclusters probed by NMR spectroscopy. *ACS Nano* **2011**, *5*, 8935–8942.

[60] Knoppe, S.; Azoulay, R.; Dass, A.; Bürgi, T. In situ reaction monitoring reveals a diastereoselective ligand exchange reaction between the intrinsically chiral $Au_{38}(SR)_{24}$ and chiral thiols. *J. Am. Chem. Soc.* **2012**, *134*, 20302–20305.

[61] Devadas, M. S.; Bairu, S.; Qian, H.; Sinn, E.; Jin, R.; Ramakrishna, G. Temperature-dependent optical absorption properties of monolayer-protected Au_{25} and Au_{38} clusters. *J. Phys. Chem. Lett.* **2011**, *2*, 2752–2758.

[62] Negishi, Y.; Igarashi, K.; Munakata, K.; Ohgake, W.; Nobusada, K. Palladium doping of magic gold cluster $Au_{38}(SC_2H_4Ph)_{24}$: Formation of $Pd_2Au_{36}(SC_2H_4Ph)_{24}$ with higher stability than $Au_{38}(SC_2H_4Ph)_{24}$. *Chem. Commun.* **2012**, *48*, 660–662.

[63] Kumara, C.; Dass, A. AuAg alloy nanomolecules with 38 metal atoms. *Nanoscale* **2012**, *4*, 4084–4086.

[64] Ferrando, R.; Jellinek, J.; Johnston, R. L. Nanoalloys: From theory to applications of alloy clusters and nanoparticles. *Chem. Rev.* **2008**, *108*, 845–910.

[65] Qian, H.; Jin, R. Controlling nanoparticles with atomic precision: The case of $Au_{144}(SCH_2CH_2Ph)_{60}$. *Nano Lett.* **2009**, *9*, 4083–4087.

[66] Qian, H.; Jin, R. Ambient synthesis of $Au_{144}(SR)_{60}$ nanoclusters in methanol. *Chem. Mater.* **2011**, *23*, 2209–2217.

[67] Kumara, C.; Dass, A. $(AuAg)_{144}(SR)_{60}$ alloy nanomolecules. *Nanoscale* **2011**, *3*, 3064–3067.

[68] Koivisto, J.; Malola, S.; Kumara, C.; Dass, A.; Häkkinen, H.; Pettersson, M. Experimental and theoretical determination of the optical gap of the $Au_{144}(SC_2H_4Ph)_{60}$ cluster and the $(Au/Ag)_{144}(SC_2H_4Ph)_{60}$ nanoalloys. *J. Phys. Chem. Lett.* **2012**, *3*, 3076–3080.

[69] Malola, S.; Häkkinen, H. Electronic structure and bonding of icosahedral core–shell gold–silver nanoalloy clusters $Au_{144-x}Ag_x(SR)_{60}$. *J. Phys. Chem. Lett.* **2011**, *2*, 2316–2321.

[70] Xie, S.; Tsunoyama, H.; Kurashige, W.; Negishi, Y.; Tsukuda, T. Enhancement in aerobic alcohol oxidation catalysis of Au_{25} clusters by single Pd atom doping. *ACS Catal.* **2012**, *2*, 1519–1523.

[71] Kurashige, W.; Munakata, K.; Nobusada, K.; Negishi, Y. Synthesis of stable Cu_nAu_{25-n} nanoclusters (n = 1–9) using selenolate ligands. *Chem. Commun.* **2013**, *49*, 5447–5449.

[72] Yao, H.; Miki, K.; Nishida, N.; Sasaki, A.; Kimura, K. Large optical activity of gold nanocluster enantiomers induced by a pair of optically active penicillamines. *J. Am. Chem. Soc.* **2005**, *127*, 15536–15543.